Available online at www.sciencedirect.com
SCIENCE DIRECT®
Geochimica et Cosmochimica Acta 70 (2006) 1113–1127
Geochimica
www.elsevier.com/locate/gca

Defect distribution and dissolution morphologies on low-index surfaces of α-quartz

Svetlana V. Yanina [a,*], Kevin M. Rosso [a], Paul Meakin [b]

[a] *Pacific Northwest National Laboratory, P.O. Box 999, MSIN K8-96, Richland, WA 99352, USA*
[b] *Idaho National Laboratory, P.O. Box 1625, Mail Stop 2025, Idaho Falls, ID 83415, USA*

Received 5 July 2005; accepted in revised form 3 November 2005

Abstract

The dissolution of prismatic and rhombohedral quartz surfaces by KOH/H_2O solutions was investigated by atomic force microscopy. Rates of dissolution of different classes of surface features (e.g., steps, voids, and dislocation etch pits) were measured. The prismatic surface etched almost two orders of magnitude faster than the rhombohedral surface, mostly due to the difference in the number and the rate of dissolution of extended defects, such as dislocations. Because of the presence of imperfect twin boundaries, defect densities on the prismatic surface were estimated at 50–100 μm^{-2}, whereas the rhombohedral surface possessed only ~0.5–1.0 μm^{-2}, mostly in the form of crystal voids. Crystal voids etched almost one order of magnitude faster on the prismatic surface than on the rhombohedral surface due to differences in the number and the density of steps formed by voids on the different surfaces. In the absence of extended defects, both surfaces underwent step-wise dissolution at similar rates. Average rates of step retreat were comparable on both surfaces (~3–5 nm/h on the prismatic surface and ~5–10 nm/h on the rhombohedral surface). Prolonged dissolution left the prismatic surface reshaped to a hill-and-valley morphology, whereas the rhombohedral surface dissolved to form coalescing arrays of oval-shaped etch pits.

1. Introduction

Quartz is among the most common minerals found in the Earth's crust (Correns et al., 1969). Unlike many other minerals, it dissolves and precipitates under mild conditions in a wide variety of aqueous environmental systems (Bennett, 1991; Bavestrello et al., 1995; Bolton et al., 1996; Schulz and White, 1999; Bennett et al., 2001; Wagner and Jochum, 2002; Gaylarde and Gaylarde, 2004; Greenwood et al., 2005). Quartz dissolution has consequently been the subject of multiple studies (see, e.g., Rimstidt and Barnes, 1980; Dove and Elston, 1992; House and Orr, 1992; Dove and Rimstidt, 1994; Dove, 1994, 1995, 1999; Tester et al., 1994; Hajash et al., 1998; Duval et al., 2002; Greenwood et al., 2005).

Most works were performed using bulk materials (e.g., sand and crushed crystals) that usually have complex surface geometries (e.g., Rimstidt and Barnes, 1980; Brady and Walther, 1990; Dove and Elston, 1992; Dove and Rimstidt, 1994; Jendoubi et al., 1998; Dove, 1999; Alekseyev et al., 2003). These studies have provided useful insight into the dissolution behavior of quartz crystals with realistic surfaces; however, they did not differentiate between the contribution of specific classes of surface morphological features (such as facets of various crystallographic orientations, crystal voids, etc.) to the 'bulk' rate laws obtained. In some cases, successful attempts have been made to reduce the bulk rate laws to rate laws derived for single-crystal surfaces dissolved under similar conditions (Gratz and Bird, 1993a,b; Dove et al., 2005). The applicability of single-crystal rate laws to more complex systems has been credited to two factors. First, fracture morphologies, which are usually thought to represent surface morphologies of sand and crushed-rock particles, have been shown to consist of a vari-

* Corresponding author. Fax: +1 509 376 3650.
E-mail address: svetlana.yanina@pnl.gov (S.V. Yanina).

0016-7037/$ - see front matter © 2005 Elsevier Inc. All rights reserved.
doi:10.1016/j.gca.2005.11.019

ety of low-index surfaces, most often rhombohedral as well as other smaller, low-index facets, including the basal and prismatic surfaces (Bloss and Gibbs, 1963; Reuschle and Darot, 1996). Second, it has been argued that, on the unit-cell scale, quartz dissolution could be described in terms of common steps e.g., the hydration of the dangling bonds and the subsequent detachment of the SiO_4 tetrahedra from various surface positions (Gallei and Parks, 1972; Gratz and Bird, 1993a,b; Xiao and Lasaga, 1996; Koretsky et al., 1997; Koretsky et al., 1998; Dove et al., 2005) regardless of the specifics of the geometry of the dissolving crystal face.

Perhaps unfairly, morphologies of quartz surfaces have received considerably less attention than did quartz 'bulk' dissolution kinetics. Until recently, surface studies of quartz have relied on visible-light and scanning electron microscopy (Gratz et al., 1990; Gratz and Bird, 1993a) as the means to observe surface morphologies. Although performed with high accuracy, visible-light measurements were limited to large etch pits ('negative crystals') formed on the sites of extended crystal defects and defect arrays (Gratz and Bird, 1993a). While large pits often dominate the morphologies of quartz surfaces (Gault, 1949; Gratz and Bird, 1993a), the size and distribution of the defects giving rise to these pits is not uniform and may vary widely from crystal to crystal or even from one area of the same crystal to another, depending on the growth history of the crystal and the characteristics of the surrounding matrix (Gault, 1949), which may potentially limit the utility of the rate laws obtained for them. Meanwhile, dissolution morphologies of the surfaces enclosing such defects remain virtually unknown. The goal of this paper is to characterize the dissolution behavior of these surfaces in detail.

2. Experimental

This study used a natural α-quartz crystal from Herkimer County, USA (a 'Herkimer diamond'). The crystal was transparent and possessed large and optically smooth prismatic and rhombohedral faces. It was cut into $2 \times 2 \times 2$ mm samples with a low-speed wafering saw so that each piece had one surface parallel to either a prismatic (1 0 0) or a rhombohedral (1 0 1) crystal surface. The surfaces of the samples were polished to a high-quality finish ($\sigma_{rms} = 0.3$–2.5 nm) using a variety of aluminum oxide pastes (final grit size was 25 nm), then cleaned in acetone, methanol, and deionized H_2O to remove polishing debris. Prismatic and rhombohedral surfaces thus obtained deviated by 1.0–1.5° (judging by their step densities) from their nominal crystallographic orientation. X-ray photoelectron spectroscopy performed using a monochromatic Al anode (Kratos Axis 165, Kratos Analytical, New York, USA) showed that samples contained 0.7–4.3% Na (the Na content varied slightly from sample to sample). The comparison of the results of the low- and the high-angle XPS analyses showed that the surface Na content matched the bulk Na content of the crystal.

Dissolution in aqueous KOH solution was performed in the following way: the samples were immersed in 0.01 M KOH (20 mL volume using deionized water) in a Teflon reaction vessel and covered with a Teflon lid. The covered vessel was placed into a pre-heated stainless-steel acid digestion bomb (Parr Instrument Company, Moline, USA). For the purpose of monitoring the internal temperature, a type-K thermocouple (Omega Engineering, Stamford, USA) was placed in contact with the lid of the vessel in the interior of the bomb. The bomb was tightly sealed and enclosed in a heating mantle (Barnstead International, Dubuque, USA) that was placed on an orbital shaker that moved at a rate of ~70 rpm throughout the heat-treatments. The temperature of the external bomb sheath was also monitored with a separate K-type thermocouple attached to the upper lid of the bomb. The bomb was heated to between 400 and 500 K. The main target temperature was 400 K, although at times, on other samples, we utilized higher temperatures to explore the development of certain dissolution features. Therefore, the dissolution temperature is implied to be 400 K unless otherwise noted. The temperature measurement limit of error was ±2 K. The heating ramp usually took ~10–15 min. Run durations varied between 2 and 20 h. During a run, the temperature of the vessel inside the bomb did not deviate from the temperature of the external bomb sheath by more than ±2 K. Upon completion of a run, the bomb was cooled in cold streaming water. The average cool-down time was 1–2 min.

After the bomb had been cooled to room temperature, the sample was taken out of the KOH solution and placed into a stream of deionized H_2O for 10–15 min to help remove the products of the reaction. The sample was then allowed to dry in air and was placed into the AFM chamber for examination. In certain cases, when AFM imaging showed that the surface of the sample retained excessive quantities of gelled reaction products, the sample was immersed in a 20 M solution of KOH for 15–30 min at room temperature and then washed in deionized H_2O for 1–3 h. Runs of selected samples were repeated in 2–20 h increments for up to 20 cycles (200 h total), with selected areas re-imaged in the AFM after each run at identical surface locations.

AFM imaging was performed in air at room temperature in contact mode using a Digital Instruments BioScope III (Veeco Instruments, Santa Barbara, USA) with Si_3N_4 and oxide-sharpened Si cantilevers with nominal spring constants of 0.8–1.2 N/m.

3. Results

3.1. Initial surfaces

Naturally occurring α-quartz exhibits several stable low-index surfaces, such as prismatic, rhombohedral, and a variety of higher index faces that are usually smaller in size (Correns et al., 1969). The basal (0 0 1) orientation is the

most stable low-index surface (Ernsberger, 1960; de Leeuw et al., 1999; Rignanese et al., 2000). It is also the fastest-growing (Ernsberger, 1960); as such, it is often not expressed in quartz crystals (Correns et al., 1969). When formed, it tends to exhibit a rough stepped morphology (Correns et al., 1969), which naturally hinders microscopic observations of its dissolution dynamics. For these reasons, it was excluded from this study. (Here and below, Miller *hkl* notation will be used to denote crystallographic planes and orientations. For comparison purposes, the basal plane is the (0001) plane in the traditional, but redundant, Miller–Bravais *hkil* notation, the prismatic planes are the $\{10\bar{1}0\}$ planes and the rhombohedral planes are the $\{10\bar{1}1\}$ planes).

The rhombohedral and prismatic surfaces follow the basal surface as the second and the third most stable quartz surfaces (de Leeuw et al., 1999). Their smooth terrace-and-step morphologies make them an attractive target for surface dissolution studies, especially since most naturally occurring quartz crystals exhibit large smooth facets of both of these orientations, even when twinned (Gault, 1949). Both surfaces do not reconstruct at temperatures below the α–β transition (Bart et al., 1992) but the ab initio calculations and the X-ray reflectivity studies show that they may undergo some vertical relaxation (de Leeuw et al., 1999; Schlegel et al., 2002).

The morphology of the polished prismatic and rhombohedral surfaces used in this study appeared essentially featureless, with small numbers of unevenly distributed large (>100 nm in lateral dimensions) defects persisting through the polishing procedure, such as faceted crystal voids. (Fig. 1A). The root-mean-square roughness (σ_{rms}) of the polished surfaces of all orientations varied from ~0.3 nm for 1-μm images to 1.5–2.5 nm for the 50-μm images. The voids accounted for most of the roughness variation between small-scale and the large-scale images of these initial surfaces.

Runs in deionized H_2O at 400 K for 24 h removed the amorphous silica layer from the polished surfaces, revealing, for both surface orientations, terrace-and-step morphologies. The average step height on the rhombohedral surface was $\sim 3.3 \pm 0.5$ Å, which is close to the distance between the nearest-neighbor rhombohedral planes in the quartz structure ($d_{[10\bar{1}]} = 3.4$ Å (Schlegel et al., 2002)). Step alignment on the rhombohedral surface was coincident with the $[\bar{2}\bar{3}2]$ direction (Fig. 1B), which is a line of intersection between the rhombohedral $\{10\bar{1}\}$ planes in quartz (Schlegel et al., 2002). The rhombohedral $\{10\bar{1}\}$ quartz surface is thought to consist of SiO_4 tetrahedra, each of which possesses a single unsaturated Si–O bond extending out of the surface plane (Ernsberger, 1960; de Leeuw et al., 1999). The 3.3-Å steps are thought to be bounded by SiO_4 tetrahedra possessing two dangling oxygen bonds each (Ernsberger, 1960; Mullins and Hirth, 1963; Schlegel et al., 2002). These doubly unsaturated SiO_4 tetrahedra have been proposed as the structural units that detach during dissolution and attach during growth (Ernsberger, 1960; Mullins and Hirth, 1963).

The direction of step alignment on the prismatic surface was close to [001] (i.e., the line of intersection between the (100) and the (011) planes). The average step height on the prismatic surface was $\sim 4.2 \pm 0.5$ Å, which is close to the distance between the nearest-neighbor prismatic planes in the quartz structure ($d_{[100]} = 4.4$ Å (Gratz et al., 1991; Schlegel et al., 2002)).

Prismatic {100} quartz surfaces can form two possible terminations. The more stable termination exposes the SiO_4 tetrahedra with one Si–O dangling bond each, while the other, less stable, termination is formed by SiO_4 tetrahedra with two dangling bonds each (Ernsberger, 1960; Mullins and Hirth, 1963; Bart et al., 1992; de Leeuw et al., 1999; Schlegel et al., 2002). The more stable structure is usually considered to be predominant (Ernsberger, 1960; Mullins and Hirth, 1963; de Leeuw et al., 1999; Schlegel

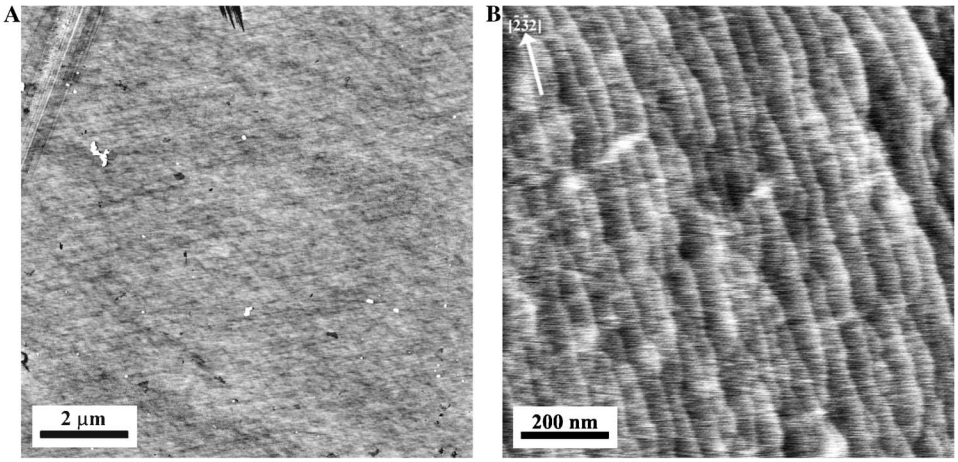

Fig. 1. (A) An initial prismatic quartz surface after cleaning. Dark 'dots' randomly distributed throughout the image are extended crystal defects. White irregularly shaped structures are the polishing debris. The height scale in the image is 50 nm; (B) an initial rhombohedral quartz surface after removal of amorphous silica polishing debris. The surface has the terrace-and-step morphology. The average step height is ~3.3 Å, or $d_{[10\bar{1}]}$. The steps are aligned close to the $[\bar{2}\bar{3}2]$ crystallographic direction. White streaks in the image are the remnants of the polishing debris. The height scale in the image is 5 nm.

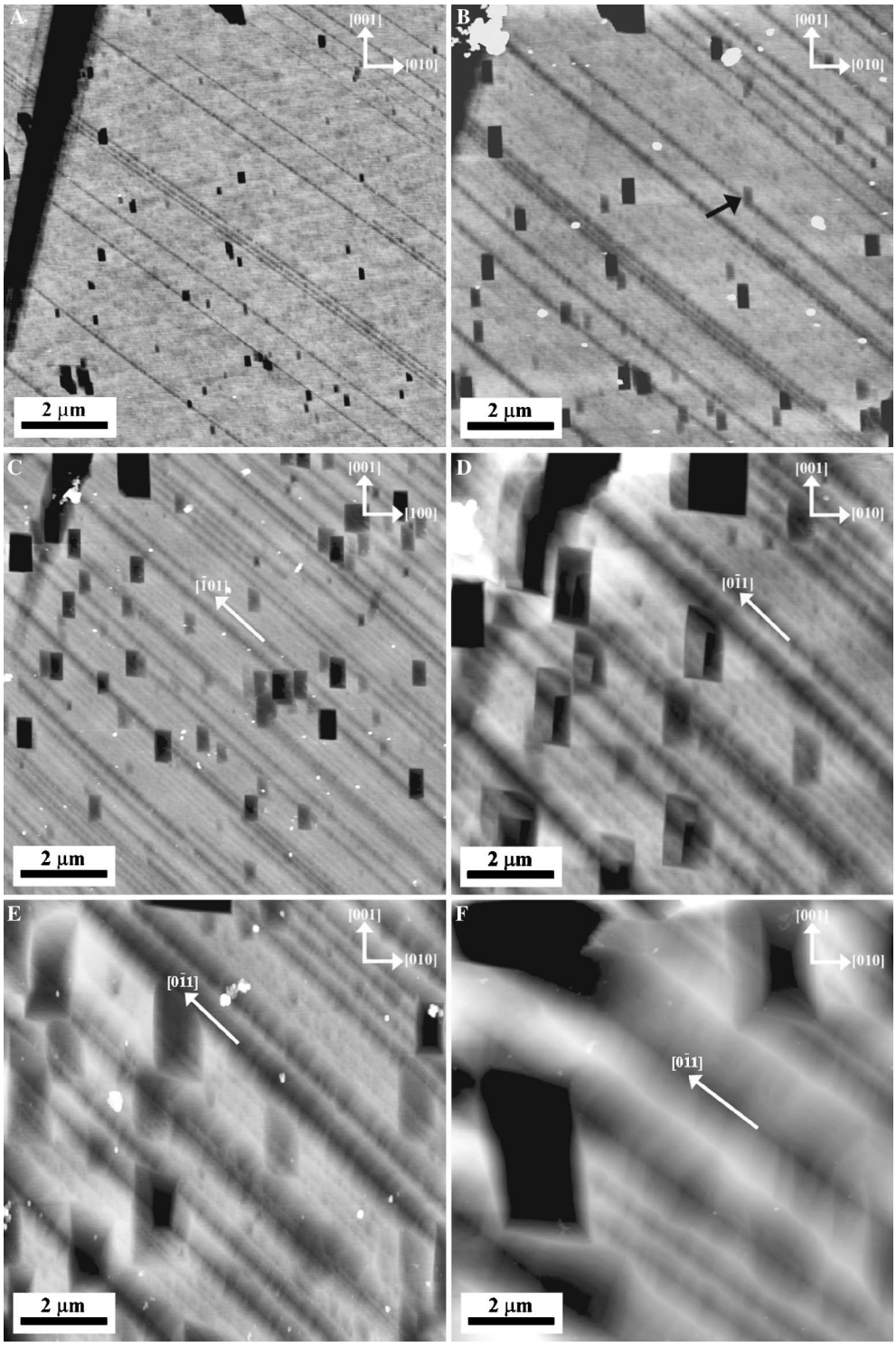

Fig. 2. The area on the prismatic surface shown in Fig. 1A, recorded after the surface has been treated for (A) 6 h in 0.01 M KOH at 400 K. The randomly distributed extended crystal defects gave rise to rectangular pyramidal pits; (B) 16 h in 0.01 M KOH at 400 K. The active (pyramidal) etch pits are seen as black rectangles; the inactive (concave) etch pits are seen as gray rectangles. Black arrow marks one of the isolated etch pits that has flattened out (become concave). White globular objects are the gelled products of the reaction; (C) 35 h in 0.01 M KOH solution at 400 K. The active (pyramidal) etch pits are seen as black rectangles; the inactive (concave) etch pits are seen as gray rectangles. The gray stripes intersecting the image from the upper left to the lower right corner are rows of etch pits. (D) 45 h in 0.01 M KOH at 400 K. Most of the large isolated etch pits seen in the image are inactive (concave). Some of the pits contain secondary pits within. The pit-rows cover 100% of the surface. The individual pits in the pit-rows are seen as 'ties' intersecting the rows; (E) 60 h in 0.01 M KOH at 400 K. Most of the large isolated etch pits seen in the image are inactive (concave). The pit-rows have undergone repetitive coarsening and are now 300–700 nm wide; (F) 95 h in 0.01 M KOH at 400 K. The pit-rows have undergone further coarsening and are now 750–1500 nm wide. The individual pits in the pit-rows are seen as 'dips' inside the rows. Most of the isolated etch pits seen in images A–E have been fully etched out. The isolated pits that are still visible have repeatedly nucleated secondary and/or tertiary etch pits (inside the 'parent' etch pits) that are still active. The height scale in images A–D is 50 nm, and in images E–F it is 100 nm.

et al., 2002), although there is some evidence that the other termination may also be observed (Schlegel et al., 2002). Similar to the rhombohedral steps, the 4.2-Å steps formed by the predominant termination on the rhombohedral surface are thought to consist of doubly unsaturated SiO_4 tetrahedra (Ernsberger, 1960; Mullins and Hirth, 1963; Schlegel et al., 2002).

The average terrace widths measured on surfaces of either orientation were comparable, at 30–50 nm. Given that these surfaces have been formed by polishing, the widths were not directly related to the pattern of crystal growth, but, rather, reflected the misalignment (1–1.5°) between the planes in the crystal and the polishing plane.

3.2. Dissolution of the prismatic surface

Dissolution of either surface led to several classes of morphological features each with its own distinct dissolution behavior. On the prismatic surface, one such class consists of isolated rectangular pits originating at pre-existing crystal voids and other defects such as dislocation tangles intersecting the surface plane. During the first 2–10 h of reaction, dissolution within crystal voids changed their shapes to a rectangular pyramid with pit edges at the surface aligned close to the [0 0 1] and the [0 1 0] directions (Figs. 2A and 3). Quartz has an enantiomorphic structure;

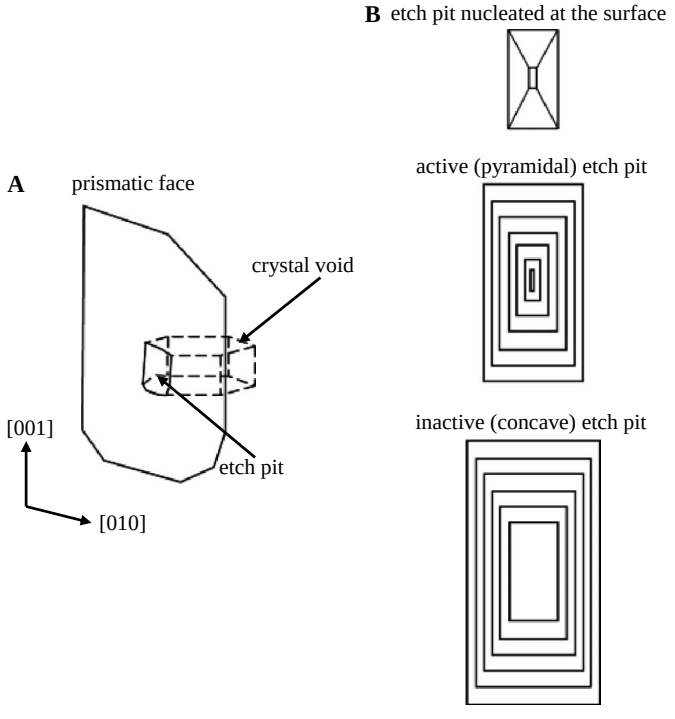

Fig. 3. The structure of etch pits on the prismatic surface. (A) A void emerging on the prismatic surface. (B) The evolution of an etch pit on the site of a crystal void on the prismatic surface. Initially, the pit is faceted to a truncated rectangular shape. The edges of the pit are aligned along the [1 0 0] and the [0 1 0] directions. In the active stage, the four sides of the pit have formed step trains. In the inactive (concave) stage, the bottom of the pit is flat.

the right-handed truncation of rectangular pit openings indicated that the right-handed form was dominant in the area where we collected images. The pits rapidly grew both laterally and in depth for the first 15–20 h after their formation. We refer to this stage of pit growth as the 'active' stage. Pit volumes were calculated as follows: the pits were assumed to have rectangular pyramidal shape. Pit openings (measured from AFM images) served as pyramid bases, while pit depths (also measured from AFM images) served as pyramid heights for the purpose of pit volume calculations. The best-fit for the pit volume (V^{pit}, in μm^3) growth trend was the power law (see Fig. 4).

$$V_{\text{P}}^{\text{pit,a}}(t) = V^{\text{void}} + \gamma_{\text{P}}^{\text{pit,a}} \cdot t^{(1.77\pm0.2)} = V^{\text{void}} + (1.61 \pm 1) \times 10^{-4} \cdot t^{(1.77\pm0.2)}, \quad (1)$$

where t is time in hours, $\gamma_{\text{P}}^{\text{pit,a}}$ is best-fit coefficient in $\mu m^3\ h^{-1.77}$, the superscript 'a' refers to the active stage of pit growth, the subscript 'P' refers to the prismatic surface, and V^{void} is the volume of the crystal void at the apical part of the pit. After 15–20 h, the pits usually lost their apices and attained concave shapes (see Figs. 2B and F and Fig. 3). The concave pits continued lateral growth by step retreat, albeit slower than their earlier pyramidal counterparts; their deepening usually stagnated (see insert in Fig. 4). Thus, we consider the initial pyramidal growth of these pits to be the active stage, and the subsequent lateral growth of concave pits as the inactive stage. The pyramidal-to-concave pit transformation appeared to mark the point at which the defects that gave rise to the pits were fully consumed. The density of the defects on the prismatic surface could therefore be estimated by counting the pyramidal pits. It stayed roughly constant at 0.25–1.00 μm^{-2} through 200 h of reaction. After the removal of defects from pit cores, any further pit enlargement proceeded through step-wise dissolution, and not through the generation of new steps that would increase pit depths. Due to the absence of new ledge sources, the enlargement of concave pits was slow compared to the growth of pyramidal pits and obeyed the linear trend

$$V_{\text{P}}^{\text{pit,c}}(t) = \gamma_{\text{P}}^{\text{pit,c}} \cdot t + V_{\text{P}}^{\text{pit,a}} = (2.6 \pm 0.3) \times 10^{-4} \cdot t + V_{\text{P}}^{\text{pit,a}}, \quad (2)$$

where $V_{\text{P}}^{\text{pit,c}}(t)$ is the average volume of the concave pits on the prismatic surface measured in μm^3, t is time in hours, $\gamma_{\text{P}}^{\text{pit,c}}$ is best-fit coefficient in $\mu m^3\ h^{-1}$, the superscript 'c' refers to the concave stage of pit growth, and $V_{\text{P}}^{\text{pit,a}}$ is the volume of the pits at the time when they became concave.

After 200 h of dissolution the isolated rectangular pits covered ~60% of the surface. Surface coverage of the isolated rectangular pits is determined, in part, by the frequency at which bulk defects emerged at the surface during the dissolution. The frequency of defect emergence (η) was estimated from the frequency of nucleation of isolated etch pits that was equal to ~0.01 $\mu m^{-2}\ h^{-1}$ (i.e., for a given square micron of surface area, a new etch pit nucleated once every 100 h). The pits showed no significant coales-

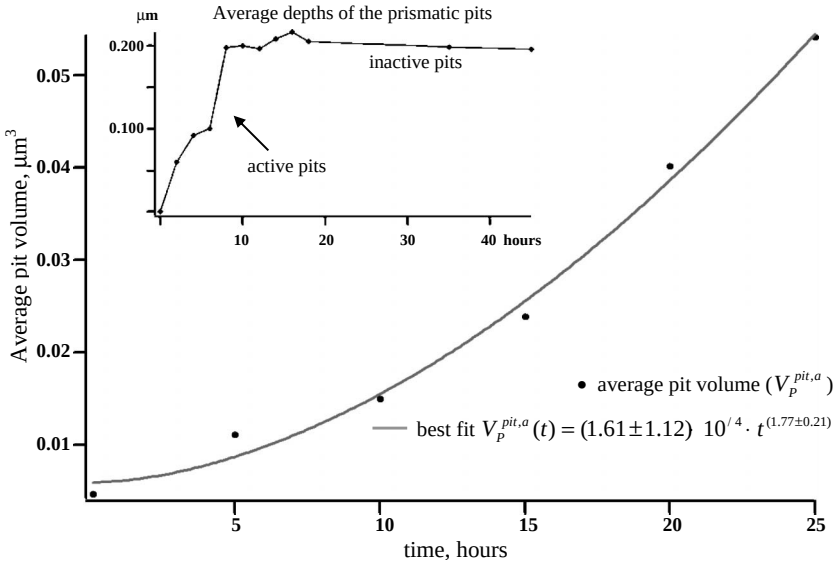

Fig. 4. Average volume of active isolated pits on the prismatic surface. Lateral dimensions and depths of active isolated pits in a selected 20×20 μm area of the prismatic surface were calculated through 25 h of the reaction. The insert shows the growth trend of all isolated pits on the prismatic surface. Depths of isolated pits in a selected 20×20 μm area of the prismatic surface were measured through 50 h of the reaction. The depths of the pits increased through 10–15 h of the reaction, and then stabilized after 20–30 h. The pits that grew depth-wise were considered active, whereas the pits with the stagnating or decreasing depths were designated inactive (concave).

cence, despite the repetitive cycles of nucleation-growth-flattening-out of isolated pits that took place every 25–40 h (Figs. 2C–F). Even on surfaces treated separately under the conditions that allowed for rapid pit expansion (such as when reacted in 5 M KOH solution at 500 K, Fig. 5), the isolated rectangular pits had not coalesced. The expansion of large etch pits has been traditionally considered as the primary driving force that determines both the dissolution rates and the dissolution morphologies of quartz crystals (Gallei and Parks, 1972; Gratz and Bird, 1993a,b; Xiao and Lasaga, 1996; Koretsky et al., 1997; Koretsky et al., 1998). Our data show, however, that pit-free areas may constitute a considerable and stable fraction of the prismatic surface. Their dissolution behavior needs to be considered when evaluating surface dissolution kinetics.

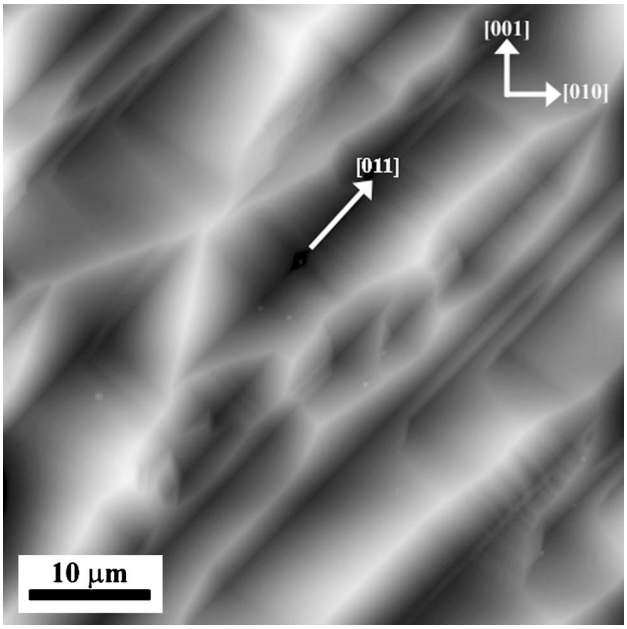

Fig. 5. The prismatic surface that has been treated for 2 h in 5 M KOH at 500 K. The repetitive coarsening of the pit-rows has created a 'hill-and-valley' morphology throughout the surface. The height scale in the image is 1 μm.

Regions of the surface where bulk defects were absent were dominated by steps, which we consider to be a second class of morphological dissolution feature on the prismatic surface. In these areas, steps that were initially straight became jagged and uneven after ~10 h of dissolution (Fig. 6). Here, dissolution involved the removal of material from steps (step-wise dissolution) while terraces stayed mostly intact, although a small number of rectangular 4.2-Å deep holes also developed (e.g., see Fig. 6). The average terrace widths in defect-free areas remained stable at 30–50 nm from 0 to 35 h of reaction, although terrace shapes gradually became highly irregular. Nevertheless, it was possible to estimate the rate of step retreat, which we did as follows: The changes in step positions were detected by comparing the positions and surface areas of terraces in 500×500 nm images of the same defect-free region that was tracked through several run cycles. The areas between the pre- and the post-treatment step positions were considered to be terrace portions that underwent dissolution during the treatments. The rate of dissolution per unit surface area (v_P^{step}, in μm/h) was obtained by multiplying the net change in the surface area of the terraces ($dS_P^{terrace}$) by the average step height (h_P^{step}) and dividing by the duration of the treatment (dt) and the total surface area of terraces tracked (S_P), which yielded

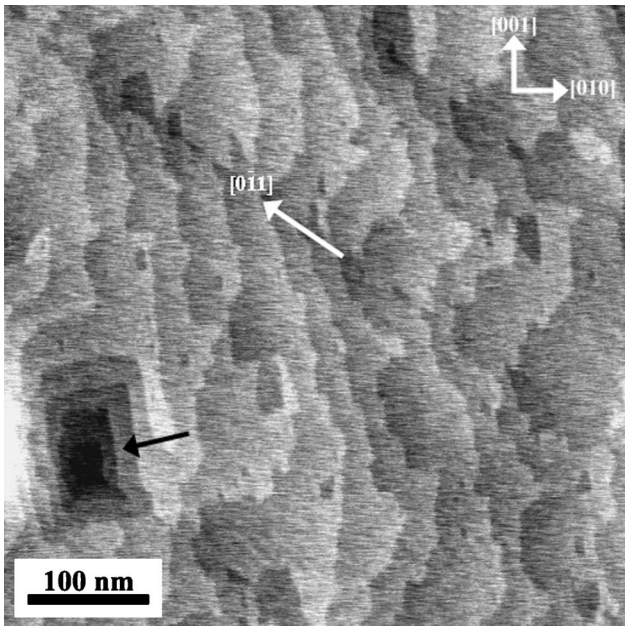

Fig. 6. The prismatic surface that has been reacted for 14 h in 0.01 M KOH at 400 K. The surface has a terrace-and-step morphology. All surface steps are 4.2*n* Å ($nd_{[1\,0\,0]}$) high, where *n* is an integer. Some terraces exhibit rectangular holes. Black arrow denotes an etch spiral formed on the site of emergence of a dislocation with a screw component. Most etch spirals seen in the image are positioned along the straight steps aligned close to the [0 $\bar{1}$ 1] direction. The height scale in the image is 5 nm.

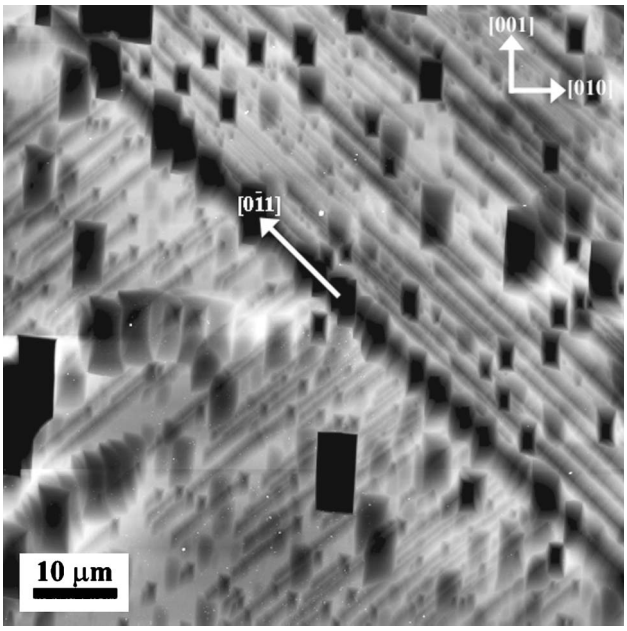

Fig. 7. The prismatic surface that has been treated for 100 h in 0.01 M KOH solution at 400 K. The pit-row alignment rotates from [0 $\bar{1}$ 1] to [0 1 1] across a larger-scale twin boundary running diagonally through the center of the image. The alignment of edges of the isolated etch pits remains virtually unchanged on either side of the boundary. The height scale in the image is 200 nm.

$$v_{\mathrm{P}}^{\mathrm{step}} = \frac{\mathrm{d}S_{\mathrm{P}}^{\mathrm{terrace}} \cdot h_{\mathrm{P}}^{\mathrm{step}}}{S_{\mathrm{P}} \cdot \mathrm{d}t} = (0.0976 \pm 0.02) \times 4.2 \times 10^{-4} = (4.10 \pm 0.6) \times 10^{-5}. \quad (3)$$

At this rate, each μm^2 of the surface lost ~300 unit cells, or 600 formula units, per second.

A third class of morphologic features that developed on the prismatic surface consisted of a large number of small (~100–150 nm in size) rectangular etch pits arranged in parallel rows aligned close to the [0 $\bar{1}$ 1] direction (Fig. 6). The pits consisted of ~4.2 Å spiral steps and appeared to have resulted from the preferential etching of dislocations with a normal to the surface component of the Burgers vector equal to $d_{[1\,0\,0]}$, or 4.2 Å. As seen in Fig. 6, the pits were often bisected by straight steps aligned along the [0 $\bar{1}$ 1] directions. In some cases, the steps appeared to have been dissolved away, leaving the pits arranged along the lines demarcating the former step locations. The nucleation, growth and coalescence of the individual etch pits on sites of these dislocations created distinct 'pit-row' morphologies; these were first observed after 7–10 h of the reaction. The direction of alignment of pit-rows rotated, usually at a ~98–103° angle, across grain boundaries in the crystal (Fig. 7). These boundaries occurred on a macroscopic length scale exceeding the 100 μm lateral range of our AFM; the length scale was estimated from visible-light microscopy observations to be ~500–1000 μm.

One possible explanation for the pit-rows is that they originated at the twin boundaries aligned close to the [0 $\bar{1}$ 1] direction in the crystal. The individual pits would have then formed due to etching of the individual dislocations that marked the boundaries. The dislocations with Burgers vectors intersecting the (1 0 0) plane would then form etch spirals on the prismatic surface. Quartz crystals are commonly twinned (Gault, 1949); both Dauphiné and Brazil penetration twins and, in particular, combinations of the two (the so-called Liebisch twins) are prevalent in Herkimer diamonds (Gault, 1949). The observed orientation and rotation of the alignment of pit-rows across the larger scale macroscopic boundaries are consistent with Brazil twinning (Fig. 7). Because of the prevalence of twinning in quartz and the apparent consistency with known quartz twin laws (Gault, 1949), we will assume that the pit-rows arise from dislocation arrays formed along twin boundaries in the crystal. As will be discussed below, the pits created by these dislocations are different from the pits associated with the crystal voids, in terms of their growth rates and their contribution to surface morphology.

The rate of removal of material from a given pit in a pit-row ($v_{\mathrm{P}}^{\mathrm{pit-row}}$, in μm^3/h) was estimated by dividing the net volume change of the pit by the duration of the treatment, which gave

$$v_{\mathrm{P}}^{\mathrm{pit-row}} = \frac{\mathrm{d}V_{\mathrm{P}}^{\mathrm{pit-row}}}{\mathrm{d}t} = (6.60 \pm 0.02) \times 10^{-6}. \quad (4)$$

The pits in pit-rows typically reached ~1.5–2.5×10^{-3} μm^2 in lateral dimensions before merging with other pits or etching out. The density of the emergent dislocations that made up the pit-rows was estimated by counting the pits and was found to be ~50–100 μm^{-2}.

The 'pit-row' morphology overtook the 'terrace-and-step' morphology as the main factor shaping the prismatic surface after ~35 h when coarsening of the pit-rows led to elimination of the original terrace-and-step landscape (Fig. 2C). Although the individual spirals in the pit-rows typically etched out within ~10–20 h, enough new dislocations usually emerged in their vicinities to maintain the pit-row geometries. Pit-row morphologies proved to dominate the morphology of the prismatic surface under the high-pH conditions also (see Fig. 4), when they had coarsened considerably already after 2 h of reaction.

Due to the coalescence of multiple individual pits into the rows, the row walls evolved into trains of zigzag steps aligned approximately parallel to the $[0\bar{1}1]$ direction. After ~35 h, the inter-step distances in the trains stabilized at ~29.4 ± 1.5 nm, and remained stable through 200 h of reaction regardless of the number of steps in the trains or the number of trains per unit surface area. Apart from dissolution at dislocation cores (i.e., the apices of the etch pits in pit-rows), dissolution inside pit-rows amounted to steady-state propagation of step trains generated by the dislocations in the rows. The rate of motion of step-trains ($v_P^{\text{step-train}}$, in μm/h) was estimated from the measurements of net changes in the positions of associated steps ($L_P^{\text{step-train}}$) over time, which gave

$$v_P^{\text{step-train}} = \frac{dL_P^{\text{step-train}}}{dt} = (2.10 \pm 0.06) \times 10^{-2}. \quad (5)$$

3.3. Dissolution of the rhombohedral surface

Like the prismatic surface, distinct morphologic classes of dissolution features could be identified on the rhombohedral surface, but in this case only two classes were found. The first class was associated with step-wise dissolution. Small-scale (⩽1 μm) images of the rhombohedral surface showed that surface steps became jagged and developed numerous kinks after 2–10 h of reaction (Fig. 8), much like the steps on prismatic surface. Dissolution in defect-free areas of the surface proceeded through step retreat; no terrace holes were ever observed through times up to 200 h. The rate of dissolution at steps on the rhombohedral surface (v_R^{step}, in μm/h) was estimated using the procedure described for the prismatic surface, from the 1 × 1 μm images of a defect-free surface region that were recorded after several dissolution runs, which gave:

$$v_R^{\text{step}} = \frac{dS_R^{\text{terrace}} \cdot h_R^{\text{step}}}{S_R \cdot dt} = (0.101 \pm 0.02) \times 3.4 \times 10^{-4} = (3.43 \pm 0.5) \times 10^{-5}. \quad (6)$$

At this rate, each μm^2 of the surface lost ~250 unit cells, or 500 formula units, per second.

The second class of dissolution feature on the rhombohedral surface consists of isolated pits originating at crystal voids. Hexagonally shaped crystal voids (Figs. 9A and 10) gave rise to trigonal pyramid pits after 2–10 h of dissolution (Figs. 9B and C and 10). Two sides of the trigonal pits consisted of facets with edges aligned along the $[\bar{2}\bar{3}2]$ and the $[2\bar{3}2]$ directions; the other pyramid side was formed by a series of wide fan-shaped steps (Fig. 10). Pit coverage of the surface stabilized at 15% after 30 h of reaction and then remained essentially unchanged through 200 h (Figs. 9D and F). Most of the pits seen on the rhombohedral surface after 200 h of treatment could be traced back to the initial crystal voids present on the starting surface, with large areas between these defects appearing essentially defect-free through all reaction times. The defect density on the rhombohedral surface was estimated to be ~0.5–1.0 μm^{-2} from pit counts. Due to the sparse pit coverage and slow pit growth, pit coarsening was considered unimportant and was neglected in estimates of the rate of surface dissolution. Only surfaces treated at higher temperatures in highly concentrated KOH solutions (e.g., at 500 K in a 5 M KOH solution, Fig. 11) showed significant coarsening of individual etch pits.

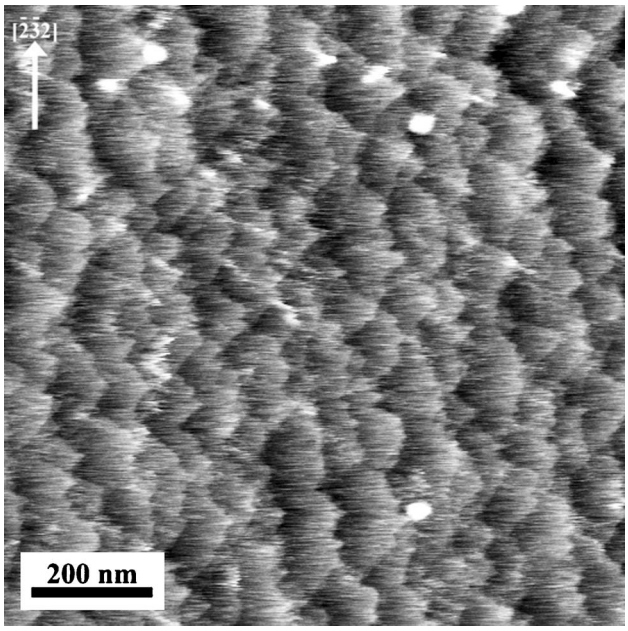

Fig. 8. The rhombohedral quartz surface that has been reacted for 2 h in 0.01 M KOH solution at 400 K. The surface has a terrace-and-step morphology. All surface steps are ~3.4 Å, or $d_{[1\,0\,\bar{1}]}$ high. The dissolution of material at steps has left them jagged. The white arrow denotes the original direction of step alignment close to $[\bar{2}\bar{3}2]$. White globular objects in the image are the remnants of the gelled products of the reaction. The height scale in the image is 5 nm.

The initial pitting and lateral pit expansion was accompanied by deepening of the pits. During this fast-growth stage (Fig. 12), pit volumes ($V_R^{\text{pit,a}}(t)$, in μm^3) followed

$$V_R^{\text{pit,a}}(t) = V^{\text{void}} + \gamma_R^{\text{pit,a}} \cdot t^{(0.64\pm0.07)} = V^{\text{void}} + (1.22 \pm 0.3) \times 10^{-4} \cdot t^{(0.64\pm0.07)}, \quad (7)$$

where again t is time in hours, $\gamma_R^{\text{pit,a}}$ is the best-fit coefficient in μm^3/h$^{0.64}$, the superscript 'a' refers to an initial 'active' stage of pit growth, and V^{void} is the volume of the void at the origin of the pit. Within 10–15 h of the nucleation,

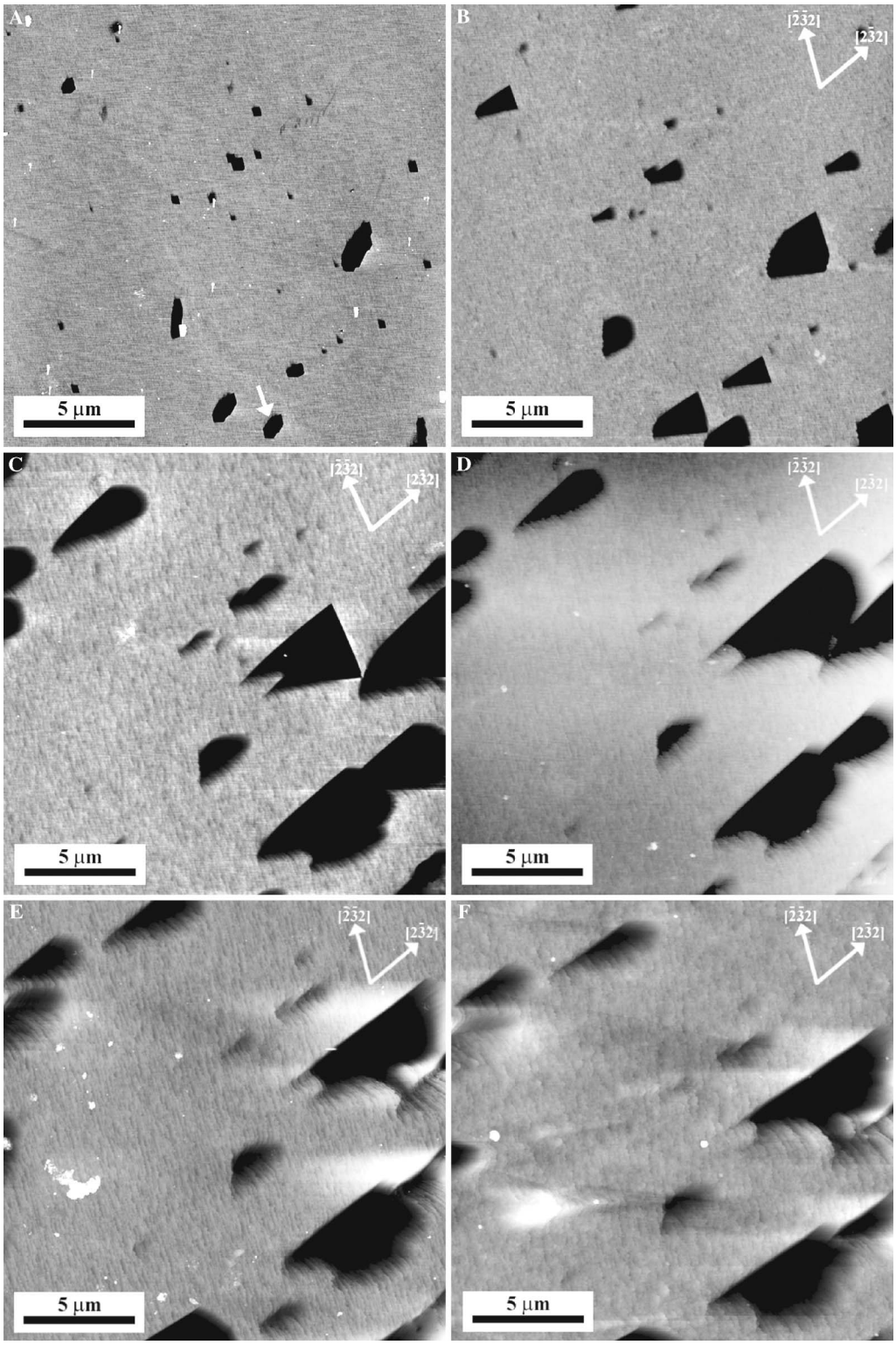

Fig. 9. (A) The rhombohedral quartz surface (A) after removal of the amorphous silica polishing debris. This is the initial condition. White arrow denotes a hexagonally faceted crystal void; (B) after the surface has been treated for 7 h in 0.01 M KOH at 400 K. The voids have refaceted to an asymmetrical trigonal pyramid shape, with the longer side aligned close to [2$\bar{3}$2]; (C) after the surface has been treated for 10 h in 0.01 M KOH at 400 K. The etch pits have grown into large shallow triangular pyramids, with a straight side aligned close to the [2$\bar{3}$2] direction; (D) after the surface has been treated for 60 h in 0.01 M KOH at 400 K. The bottoms of the etch pits have become fan-shaped; (E) after the surface has been treated for 140 h in 0.01 M KOH at 400 K. Both the number and the size of the etch pits remained essentially unchanged from 30 through 140 h of the reaction. White globular objects seen in the image are the gelled remnants of the products of the reaction; (F) after the surface has been treated for 200 h in 0.01 M KOH at 400 K. Both the number and the size of the etch pits remained essentially unchanged from 30 through 200 h of the reaction. The height scale in images A and B is 50 nm, and in images C–F it is 100 nm.

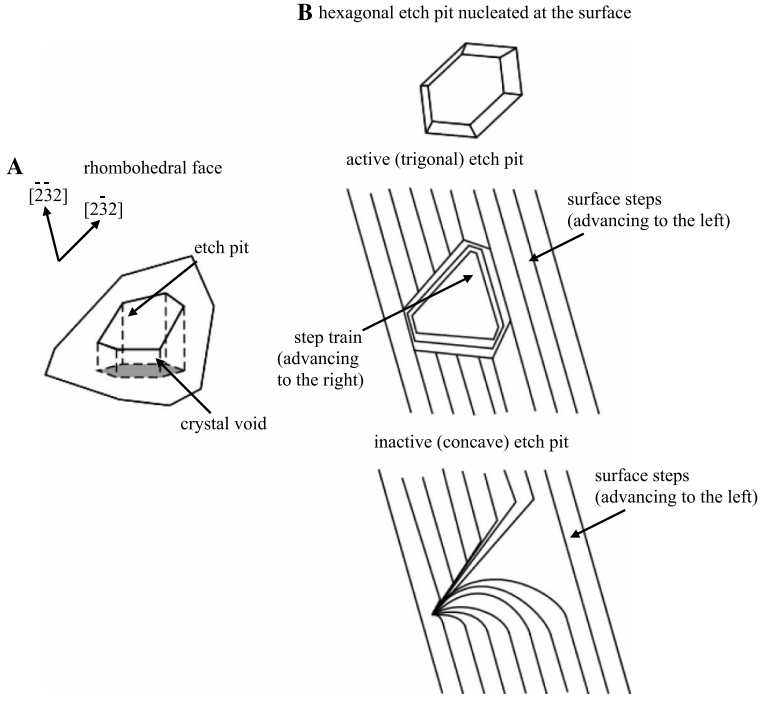

Fig. 10. The structure of etch pits on the rhombohedral surface. (A) A hexagonal void emerging on the rhombohedral surface. (B) The evolution of an etch pit on the rhombohedral surface. In the active stage, the sides of the pit have formed step trains. The steps in the trains are aligned along the $[2\bar{3}2]$ and the $[2\bar{3}2]$ directions. The step-train on one side of the pit advances in the direction opposite to the direction of advancement of the steps outside the pit and is being eliminated. In the inactive (convex) stage, the bottom of the pit is flat.

the depths of the pits usually stabilized, and the pits essentially stopped expanding laterally (Figs. 9D–F and 12). As was the case for the isolated rectangular pits on the prismatic surface, depth stabilization indicated that the defects giving rise to these pits on the rhombohedral surface had been etched out of the crystal. The evolution of the etch pits could, therefore, be separated into the active stage where fast defect etching occurred, and the inactive stage where slow growth of concave pits occurred. The slow growth of concave pits obeyed a roughly linear trend:

$$V_{\mathrm{R}}^{\mathrm{pit,c}}(t) = \gamma_{\mathrm{R}}^{\mathrm{pit,c}} \cdot t + V_{\mathrm{R}}^{\mathrm{pit,a}} = (4.31 \pm 0.4) \times 10^{-6} \cdot t + V_{\mathrm{R}}^{\mathrm{pit,a}} \mu\mathrm{m}^3, \quad (8)$$

where $V_{\mathrm{R}}^{\mathrm{pit,c}}(t)$ is the average volume of the concave pits on the rhombohedral surface measured in μm^3, t is time in hours, $\gamma_{\mathrm{R}}^{\mathrm{pit,c}}$ is the best-fit coefficient in $\mu m^3/h$, $V_{\mathrm{R}}^{\mathrm{pit,a}}$ was the pit volume by the time they became concave.

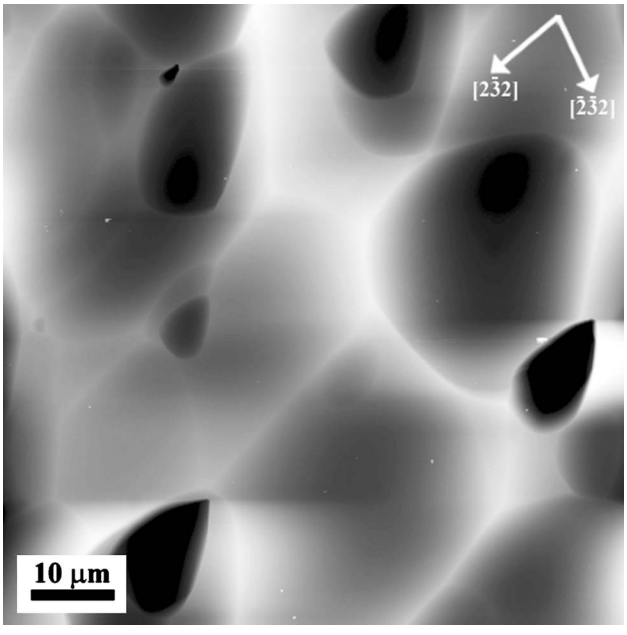

Fig. 11. The rhombohedral quartz surface that has reacted for 2 h in 5 M KOH at 500 K. The height scale in the image is 1 μm.

4. Discussion

Based on the rate analyses of the various classes of morphologic features, dissolution processes on both the prismatic and rhombohedral surfaces could be divided into two groups according to their rates: (1) step-wise dissolution and (2) active etching of dislocation cores and other extended defects. Because the growth of concave pits involved the retreat of step trains forming pit walls, expansion of concave etch pits belongs to the first group. Step-wise dissolution also encompassed both the etching of the jagged steps and the motion of step-trains on the prismatic surface, although the two had different characteristic rates.

The rates of step-wise dissolution in defect-free areas on both quartz surfaces were comparable [$\sim 4.0 \times 10^{-5}$ μm/h on the prismatic surface, and $\sim 3.5 \times 10^{-5}$ μm/h on the rhombohedral surface, see Eqs. (3) and (6)]. Given that, on average, defect-free areas of the prismatic surface contained

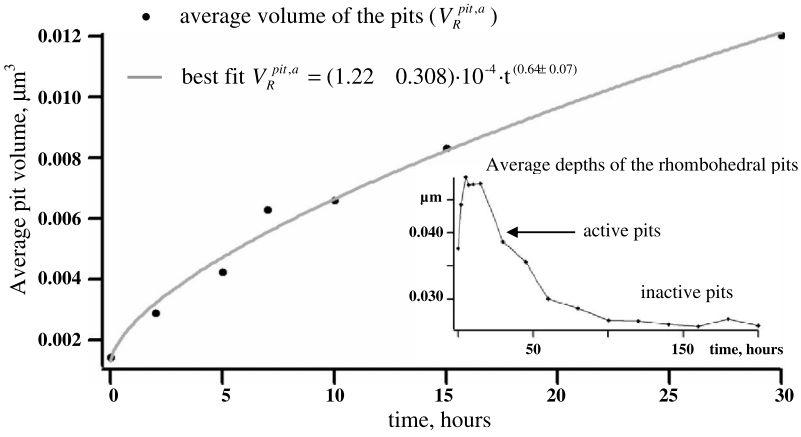

Fig. 12. Average volume of active isolated pits on the rhombohedral surface. Lateral dimensions and depths of active isolated pits in a selected 20 × 20 μm area of the rhombohedral surface were measured through 30 h of the reaction. The volumes of the pits were calculated using the assumption that the pits were trigonal pyrimidal in shape. The insert shows the depth trend of all isolated pits on the rhombohedral surface were measured through 200 h of the reaction. The depths of the pits rose from 0 to ~10–15 h of the reaction, and then started falling after 20–30 of the reaction. The pits that grew depth-wise were considered active, whereas the pts with the stagnating or decreasing depths were considered inactive (concave).

20–33 steps per micron, the average rate of retreat of an individual step on it was ~3.0–5.0 nm/h. The rhombohedral surface contained approximately 10–20 steps per micron, and the rate of step retreat on it was ~5.0–10 nm/h. In these calculations, step retreat is assumed to occur only in the direction normal to the nominal direction of step alignment, i.e., normal to the [0 0 1] direction on the prismatic surface and normal to the $[\bar{2}\,\bar{3}\,2]$ direction on the rhombohedral surface. The increasing irregularity of step shapes, however, rendered both step widths and step velocities of limited use for the purpose of characterizing surface dynamics.

Although no data on energies of stepped quartz surfaces are available at present, the kinetic model of quartz dissolution in alkali aqueous solutions proposed by Gratz and Bird (1993a) suggests that reaction mechanisms and the sites responsible for dissolution (the SiO_4 groups that possess a pair of dangling bonds each) should be similar, if not identical, on both surfaces. The ab initio simulations of vacuum-terminated defect-free surfaces of α-quartz performed by de Leeuw et al. (1999) indicate that the free energy of the rhombohedral surface (2.34 J/m^2) should be somewhat lower than the free energy of the prismatic surface (2.77 J/m^2). The difference persists when water is available: the energy of the hydrated rhombohedral surface should decrease to 0.32 versus 0.39 J/m^2 for the hydrated prismatic surface (de Leeuw et al., 1999). Since it is reasonable to assume that both surfaces are fully hydrated in the KOH/H_2O solutions, their energies should be close to their calculated 'hydrated' values. Activation energies for dissolution in KOH calculated from visible-light microscopy measurements of the growth of large etch pits (negative crystals) by Gratz and Bird (1993a) are within ~4% of one another, at 90.2 kJ/mol for the rhombohedral surface and 86.4 kJ/mol for the prismatic surface. In light of these data, similar rates of step-wise dissolution reported here for the defect-free prismatic and rhombohedral surfaces are not surprising. Both de Leeuw et al. (1999) and Gratz and Bird (1993b) point out that the prismatic surface should be somewhat less susceptible to dissolution than the rhombohedral surface, and our results are in agreement with their findings.

Despite comparable step dissolution rates, the dissolution morphology of the prismatic surface became considerably rougher than the morphology of the rhombohedral surface. This observation arises from differences in the number and the nature of defects that emerged on the two surfaces. The average density of extended defects in α-quartz is usually between 10^{-3}–10^2 per μm^2 (Liu et al., 1995); for example, defect densities in crystals used in the work of Gratz and Bird (1993a) were at the lower end of this range. Hence, it is reasonable to expect that defect-free areas would not be common on any of the stable quartz surfaces. Indeed, the density of extended defects on the initial quartz surfaces used in this work was determined to be 0.25–1 μm^{-2}, in addition to the defects that were revealed by etching. Since the contribution of defect-free areas to the dissolution process was constant and similar on both surfaces throughout the reaction, any variation in the rate of dissolution between the prismatic and rhombohedral surfaces should have depended mostly on variations in the number and the nature of defects.

On the rhombohedral surface, the newly emerged defects usually etched out approximately within the first 10 h after their appearance at the surface (Figs. 9A and B). Therefore, the amount of material etching out during the 'active' stage of pit development can be written as

$$V_{\mathrm{R}}^{\mathrm{pit,a}} = V_{\mathrm{R}}^{\mathrm{pit,a}}|_{t=10} = -V_{\mathrm{R}}^{\mathrm{pit,a}}|_{t=0} = \gamma_{\mathrm{R}}^{\mathrm{pit,a}} \cdot (10^{(0.64\pm0.07)} - 0) = (1.22 \pm 0.3) \times 10^{-4+(0.64\pm0.07)} \cong (5.42 \pm 1) \times 10^{-4}. \quad (9)$$

Here, again, $V_{\mathrm{R}}^{\mathrm{pit,a}}$ is the volume of the active pits on the rhombohedral surface in μm^3, t is time in hours, and $\gamma_{\mathrm{R}}^{\mathrm{pit,a}}$ is the best-fit coefficient in μm^3/h$^{0.64}$.

The frequency of emergence of new extended defects (η) was taken to be equal to the frequency of nucleation of isolated etch pits at quartz surfaces and was estimated at $\sim 0.01\ \mu m^{-2}\ h^{-1}$. The average rate of dissolution inside the active isolated pits on the rhombohedral surface ($v_R^{pit,a}$, in μm/h) could therefore be estimated using

$$v_R^{pit,a} = \eta \cdot V_R^{pit,a} = 0.01 \times (5.42 \pm 1) \times 10^{-4} = (5.42 \pm 1) \times 10^{-6}. \quad (10)$$

Active isolated pits on the prismatic surface similarly etched out within 10–15 h of their emergence (Fig. 4). Ignoring the initial volumes of the voids at the pits' origins, the amount of material dissolving inside active isolated pits on the prismatic surface ($V_P^{pit,a}$, in μm^3) could be estimated using Eq. (3) and the average lifetime of active pits, which gives

$$V_P^{pit,a} = V_P^{pit,a}|_{t=10} - V_P^{pit,a}|_{t=0} = \gamma_P^{pit,a} \cdot (10^{(1.77\pm0.2)} - 0) = (1.61 \pm 1) \times 10^{-4} \times 10^{(1.77\pm0.2)} \cong (1.33 \pm 1) \times 10^{-2}. \quad (11)$$

Here, $V_P^{pit,a}$ is the volume of the active pits on the prismatic surface in μm^3, t is time in hours, and $\gamma_P^{pit,a}$ is the best-fit coefficient in $\mu m^3/h^{0.64}$. The average rate of dissolution of material inside active isolated pits on the prismatic surface ($v_P^{pit,a}$, in μm/h) is then

$$v_P^{pit,a} = \eta \cdot V_P^{pit,a} = 0.01 \times (1.33 \pm 1) \times 10^{-2} = (1.33 \pm 1) \times 10^{-4}. \quad (12)$$

Surface pit coverage essentially stabilized after ~20–30 h on both surfaces. At this point, isolated pits (at least 80% of which were inactive at any given time, i.e., concave) covered ~60% of the prismatic surface. On the rhombohedral surface, isolated pits (at least 90% of which at any given time were inactive) covered ~15% of the surface. Therefore, the growth of inactive pits became a steady-state process after the initial ~20–30 h of treatment. Averaging over the number of inactive pits per square unit area per unit time and using Eq. (2), the volumes of concave pits on the prismatic surface ($V_P^{pit,c}$, in μm) followed

$$V_P^{pit,c} = 0.60 \times 0.80 \cdot V_P^{pit,c}(t) = 0.54 \times (2.63 \pm 0.3) \times 10^{-4} \cdot t = (1.42 \pm 0.1) \times 10^{-4} \cdot t. \quad (13)$$

On the rhombohedral surface, the volumes of concave pits [$V_R^{pit,c}$ in μm, see Eq. (8)] followed

$$V_R^{pit,c} = 0.15 \times 0.90 \cdot V_R^{pit,c}(t) = 0.14 \times (4.31 \pm 0.4) \times 10^{-6} \cdot t = (5.82 \pm 0.6) \times 10^{-7} \cdot t. \quad (14)$$

As can be seen from Eq. (14), the rate of dissolution inside concave pits on the rhombohedral surface was very slow, at $\sim 6 \times 10^{-7}$ μm/h, and for all practical purposes, the pits stagnated. Since the overall defect density on the rhombohedral surface was also low and stable throughout, the contribution of step-wise dissolution in defect-free surface areas to the overall dissolution should be taken into account, which can be written as

$$V_R = V_R^{pit,a} + V_R^{pit,c} + V_R^{steps}. \quad (15)$$

Given that steps covered ~85% of the surface area free of pits, the dissolution rate on the rhombohedral surface v_R (in μm/h) can be derived by combining Eqs. (10), (14), and (6), which gives

$$v_R = \frac{dV_R}{dt} = v_R^{pit,a} + \frac{dV_R^{pit,c}}{dt} + v_R^{step} = (5.42 \pm 1) \times 10^{-6} + (5.82 \pm 0.6) \times 10^{-7} + 0.85 \times (3.43 \pm 0.5) \times 10^{-5} = (3.53 \pm 1) \times 10^{-5}. \quad (16)$$

As can be seen from Eq. (16), dissolution on the rhombohedral surface is dominated by the steps (~82%), with the active pits contributing ~16% and the concave pits contributing less than 2% of the overall dissolution rate. Although dissolution inside active etch pits was considerably faster than step-wise dissolution, active pits covered, on average, only a small fraction of rhombohedral surface, while step-wise dissolution occurred on at least ~85% of the surface area.

While the defect density on the rhombohedral surface fell within the low end of the range usually reported for α-quartz (Liu et al., 1995), the density of defects on the prismatic surface was closer to the upper limit of this range. The density of emergent dislocations that made up pit-rows on the prismatic surface, η^{row}, was estimated to be 50–100 μm^{-2}. Given that pit-row morphologies persisted through 200 h of the reaction, it was assumed that the density of the pit-row dislocations remained essentially unchanged through all reaction times. Since the dissolution rate inside a given pit site in a pit-row was estimated using Eq. (4), the average rate of dissolution in pit-row dislocation sites (v_P^{row}, in μm/h) could be estimated using

$$v_P^{row} = \eta_P^{row} \cdot v_P^{pit-row} = \eta_P^{row} \cdot \frac{dV_P^{pit-row}}{dt} = (75 \pm 25) \times (6.60 \pm 0.02) \times 10^{-6} = (4.95 \pm 1) \times 10^{-4}. \quad (17)$$

Due to the high-density of the pit-row dislocations, the roughness of the prismatic surface far exceeded the roughness of the rhombohedral surface within 100 h of the reaction. The pit-row morphologies covered 100% of the defect-free surface area after ~35 h of reaction, with pit occupation of the surface area given by

$$S_P^{row} = (\eta_P^{row} \cdot S_P^{pit-row}) = (75 \pm 25)\% \times (2.00 \pm 0.5) \times 10^{-3} = 16 \pm 8\% \text{ of the total surface area of the prismatic face.} \quad (18)$$

Defect-free surface areas on the prismatic surface became virtually extinct after 35 h of reaction, and step-wise dissolution amounted to the motion of step-trains initiated by etch pits along pit-rows and by the concave pits from 35 through 200 h of reaction. Given that the average velocity of step-trains was estimated to be $v_P^{step-train} = (2.10 \pm 0.06) \times 10^{-2}$ μm/h, and that the average step height (h_P^{step}) was

~4.2 Å high, the rate of dissolution calculated per 1 μm-long projected $[0\,\bar{1}\,1]$ segment ($l_P^{segment} = 1\mu m$) of a given step in a step-train could be estimated using

$$v_P^{step} = v_P^{step-train} \cdot h_P^{step} \cdot l_P^{segment} = (2.10 \pm 0.06) \times 10^{-2} \times 4.2 \times 10^{-4} \times 1 = (8.82 \pm 0.3) \times 10^{-6}, \quad (19)$$

where v_P^{step} is measured in $\mu m^3/h$. Since the average inter-step distance in step-trains was ~29.4 ± 0.5 nm, the prismatic surface contained, on average, ~34 steps per 1 μm^2. (This estimate ignores dislocation etch pits and other surface features that could have altered local step densities). Step trains were assumed to have covered the surface more or less uniformly, save for the areas covered by isolated etch pits (~60% of the surface) and etch pits arising from dislocation arrays (~16% of the surface). Step-train surface coverage, therefore, amounted to at least ~24% of the surface. The average rate of dissolution in the areas covered by step-trains could be calculated using

$$v_P^{step-train} = 0.24 \times 34 \cdot v_P^{step} = 8.16 \times (8.82 \pm 0.3) \times 10^{-6} = (7.20 \pm 0.2) \times 10^{-5}, \quad (20)$$

where $v_P^{step-train}$ is measured in μm/h.

The velocity of individual steps in step-trains was ~0.021 μm/h [see Eq. (5)]. In comparison with Gratz and Bird (1993a), the velocity of step-trains forming the walls of their 'negative crystals' reached ~0.004–0.054 μm/h for the 379–421 K temperature interval. The lateral dimensions of negative crystals (⩾100 μm in length) exceeded lateral range of our AFM and thus fell outside the scope of this work. Nevertheless, our estimates of step-train velocities are well within the range of those reported by Gratz and Bird (1993a). Our measurements of the average distance between steps in step-trains (i.e., 29.4 ± 0.5 nm) were also very close to the values of 20–25 nm reported by Gratz et al. (1991) for step-trains forming dislocation etch pits on the prismatic quartz surface.

The overall rate of dissolution on the prismatic surface (v_P, in μm/h) could be obtained by adding together the individual rates of dissolution inside pit-row dislocations, large isolated pits, and step-trains, which gave

$$v_P = v_P^{pit,a} + \frac{dV_P^{pit,c}}{dt} + v_P^{step-train} + v_P^{row} = (1.33 \pm 1) \times 10^{-4} + (1.42 \pm 0.1) \times 10^{-4} + (7.20 \pm 0.2) \times 10^{-5} + (4.95 \pm 2) \times 10^{-4} = (8.42 \pm 3) \times 10^{-4}. \quad (21)$$

As follows from Eq. (21), active isolated etch pits accounted for ~16% of the overall rate of dissolution on the prismatic surface; dislocation arrays contributed almost 59%; and the remaining 25% came from step-train motion inside concave pits and in pit-rows. The contribution of the active pits forming pit-rows to the dissolution process is commensurate with their high-density on the surface: after 35 h of the reaction, they covered at least to 25% of the prismatic surface. The active isolated pits covered, on average, about 2–5% of the surface at a time, while step-trains and the inactive pits covered the rest of the surface.

Because the rhombohedral surface did not develop pit-row morphologies, a direct comparison of the overall dissolution rates may not be very meaningful. However, it could be more informative to make comparison with the rate of dissolution on a hypothetical 'untwinned' prismatic surface, i.e., on the prismatic surface that is not covered by pit-rows. Given our analysis of the dissolution rates of the various classes of features, such a comparison is possible. Assuming that pit-row morphologies did not form, the overall dissolution rate on the hypothetical untwinned prismatic surface (v_P^s, measured in μm/h) should have included the contribution of step-wise dissolution in defect-free areas (v_P^{step}, see Eq. (3)) that would occupy ~40% of the surface left free by isolated etch pits that would, presumably, occupy the remaining 60% of the surface, which gives

$$v_P^s = v_P^{pit,a} + \frac{dV_P^{pit,c}}{dt} + 0.4 \cdot v_P^{step} = (1.33 \pm 1) \times 10^{-4} + (1.42 \pm 0.1) \times 10^{-4} + 0.4 \times (4.10 \pm 0.6) \times 10^{-5} = (2.91 \pm 1) \times 10^{-4}. \quad (22)$$

Comparison of Eqs. (21) and (22) shows that the twinned prismatic surface dissolved almost thrice as fast as the hypothetical untwinned prismatic surface, at ~8×10^{-3} versus ~3×10^{-4} μm/h, mostly because of the dissolution inside pit rows (~5×10^{-4} μm/h) that are excluded from the hypothetical untwinned surface. Dissolution of the rhombohedral surface, ($v_R \cong 3.5 \times 10^{-5}$ μm/h), was more than 20 times slower than dissolution of the twinned prismatic surface and an order of magnitude slower than the predicted dissolution rate of the hypothetical untwinned prismatic surface. Comparing the rates of dissolution of the individual classes of surface features,

Table 1
The comparison between the rates of dissolution of various classes of surface features present on quartz surfaces

	Twinned prismatic surface	Hypothetical 'untwinned' prismatic surface	Rhombohedral surface
Step-wise dissolution	0	0.16 ± 0.03	0.29 ± 0.04
Etching of active pits	1.33 ± 1	1.33 ± 1	0.054 ± 0.01
Etching of convex pits	1.42 ± 0.1	1.42 ± 0.1	0.0060 ± 0.0006
Motion of step trains	0.72 ± 0.02	0	0
Etching of dislocations in pit rows	4.95 ± 2	0	0

All rates are in 10^{-4} μm/h units.

active isolated pits on the prismatic surface dissolved almost an order of magnitude faster than did active isolated pits on the rhombohedral surface (130×10^{-6} versus $\sim 6 \times 10^{-6}$ μm/h, Table 1). Since active pits were created by the same kinds of crystal defects emerging at two different surfaces, this discrepancy is likely related to the differences in the morphologies of the pits, rather than the defects themselves. The newly formed pits on the prismatic surface typically had much narrower openings than their counterparts on the rhombohedral surface (compare, e.g., Figs. 2A and 9A): therefore, the defects that gave raise to these pits likely had shapes that were narrow and elongated along {1 0 1} planes. When emerging on the prismatic surface, such defects formed deep narrow pits; when emerging on the rhombohedral surface, the pits they formed were wide and shallow (see Figs. 3 and 10). From the geometric considerations, the defects emerging on the prismatic surface were likely to produce more steps than they did when emerging on the rhombohedral surface. The higher number of associated steps may have also boosted the rate of expansion of the concave pits on the prismatic surface. They grew at an appreciable rate ($\sim 1.4 \times 10^{-4}$ μm/h), while the concave pits on the rhombohedral surface essentially stagnated.

5. Conclusions

We investigated dissolution morphologies of the prismatic and rhombohedral surfaces of α-quartz treated in 0.01 M KOH solutions at 400 K. The prismatic surface dissolved ~100 times faster than the rhombohedral surface, mostly due to the presence of dislocations marking the emergence of extended planar defects (twin boundaries). The etching of these dislocations accounted for the removal of 50% of material dissolved on the prismatic surface. The coalescence of step spirals formed at the points of emergence of these dislocations was responsible for the 're-faceting' of the prismatic surface to the hill-and-valley morphology. Other extended crystal defects (e.g., crystal voids, isolated dislocation, etc.) also made considerable contribution to dissolution morphologies on both surfaces. These defects were responsible for almost 30% of the overall dissolution rate on the prismatic surface, and about 50% of the overall dissolution rate on the rhombohedral surface. Defect-free areas on both surfaces dissolved through the motion of surface steps. The rates of step retreat measured on both surfaces were similar, at ~3 to 10 nm/h, as expected, given the similar energetics of step-wise dissolution usually proposed for both surfaces.

Acknowledgments

This work was made possible by a grant from the U.S. Department of Energy, Office of Basic Energy Sciences, Engineering and Geosciences Division. This research was performed in part using the ambient Scanning Probe Microscopy facility at the William R. Wiley Environmental Molecular Sciences Laboratory at Pacific Northwest National Laboratory. The EMSL is funded by the Office of Biological and Environmental Research in the U.S. Department of Energy. Pacific Northwest National Laboratory is operated by Battelle for the U.S. Department of Energy under Contract DE-AC06-76RLO 1830.

Associate editor: Kathryn L. Nagy

References

Alekseyev, V.A., Medvedeva, L.S., Tatsii, Y.G., 2003. Difference in the mechanisms and rates of quartz dissolutions and precipitation at 150 °C. *Geochem. Int.* **41**, 459–466.

Bart, F., Gautier, M., Duraud, J.P., Henriot, M., 1992. (0 1 0) Alpha-quartz surface—a LEED, XANES and EELS study. *Surf. Sci.* **274**, 317–328.

Bavestrello, G., Arillo, A., Benati, U., Cerrano, C., Cattaneovietti, R., Cortesogno, L., Gaggero, L., Giovine, M., Tonetti, M., Sara, M., 1995. Quartz dissolution by the sponge Chondrosia-Reniformis (Porifera, demospongiae). *Nature* **378**, 374–376.

Bennett, P.C., 1991. Quartz dissolution in organic-rich aqueous systems. *Geochim. Cosmochim. Acta* **55**, 1781–1797.

Bennett, P.C., Rogers, J.R., Choi, W.J., 2001. Silicates, silicate weathering, and microbial ecology. *Geomicrobiol. J.* **18**, 3–19.

Bloss, F.D., Gibbs, G.V., 1963. Cleavage in quartz. *Am. Mineral.* **48**, 821–838.

Bolton, E.W., Lasaga, A.C., Rye, D.M., 1996. A model for the kinetic control of quartz dissolution and precipitation in porous media flow with spatially variable permeability: formulation and examples of thermal convection. *J. Geophys. Res. Solid Earth* **101**, 22157–22187.

Brady, P.V., Walther, J.V., 1990. Kinetics of quartz dissolution at low-temperatures. *Chem. Geol.* **82**, 253–264.

Correns, C.W., Zemann, J., Koritnig, S., 1969. *Introduction to Mineralogy, Crystallography and Petrology*. Springer, Heidelberg, New York.

de Leeuw, N.H., Higgins, F.M., Parker, S.C., 1999. Modeling the surface structure and stability of α-quartz. *J. Phys. Chem. B* **103**, 1270–1277.

Dove, P.M., 1994. The dissolution kinetics of quartz in sodium-chloride solutions at 25 to 300 °C. *Am. J. Sci.* **294**, 665–712.

Dove, P.M., 1995. Kinetic and thermodynamic controls on silica reactivity in weathering environments. In: *Chemical Weathering Rates Of Silicate Minerals,* Vol. 31, pp. 235–290.

Dove, P.M., 1999. The dissolution kinetics of quartz in aqueous mixed cation solutions. *Geochim. Cosmochim. Acta* **63**, 3715–3727.

Dove, P.M., Elston, S.F., 1992. Dissolution kinetics of quartz in sodium-chloride solutions—analysis of existing data and a rate model for 25 °C. *Geochim. Cosmochim. Acta* **56**, 4147–4156.

Dove, P.M., Rimstidt, J.D., 1994. Silica–water interactions. In: *Silica: Physical Behavior, Geochemistry And Materials Applications,* Vol. 29, pp. 259-317.

Dove, P.M., Han, N., De Yoreo, J.J., 2005. Mechanisms of classical crystal growth theory explain quartz and silicate dissolution behavior. *Proc. Natl. Acad. Sci. USA* **102**, 15357–15362.

Duval, Y., Mielczarski, J.A., Pokrovsky, O.S., Mielczarski, E., Ehrhardt, J.J., 2002. Evidence of the existence of three types of species at the quartz-aqueous solution interface at pH 0–10: XPS surface group quantification and surface complexation modeling. *J. Phys. Chem. B* **106**, 2937–2945.

Ernsberger, F.M., 1960. Structural effects in the chemical reactivity of silica and silicates. *J. Phys. Chem. Solids* **13**, 347–351.

Gallei, E., Parks, G.A., 1972. Evidence for surface hydroxyl groups in attenuated total reflectance spectra of crystalline quartz. *J. Colloid Interface Sci.* **38** (3), 650–662.

Gault, H.R., 1949. The frequency of twin types in quartz crystals. *Am. Mineral.* **34**, 142–162.

Gaylarde, P., Gaylarde, C., 2004. Deterioration of siliceous stone monuments in Latin America: microorganisms and mechanisms. *Corr. Rev.* **22**, 395–415.

Gratz, A.J., Bird, P., 1993a. Quartz dissolution—negative crystal experiments and a rate law. *Geochim. Cosmochim. Acta* **57**, 965–976.

Gratz, A.J., Bird, P., 1993b. Quartz dissolution—theory of rough and smooth surfaces. *Geochim. Cosmochim. Acta* **57**, 977–989.

Gratz, A.J., Bird, P., Quiro, G.B., 1990. Dissolution of quartz in aqueous basic solution, 106–236 °C—surface kinetics of perfect crystallographic faces. *Geochim. Cosmochim. Acta* **54**, 2911–2922.

Gratz, A.J., Manne, S., Hansma, P.K., 1991. Atomic force microscopy of atomic-scale ledges and etch pits formed during dissolution of quartz. *Science* **251**, 1343–1346.

Greenwood, J.E., Truesdale, V.W., Rendell, A.R., 2005. Toward an understanding of biogenic-silica dissolution in seawater—an initial rate approach applied between 40 and 90 °C. *Aquat. Geochem.* **11**, 1–20.

Hajash, A., Carpenter, T.D., Dewers, T.A., 1998. Dissolution and time-dependent compaction of albite sand: experiments at 100 and 160 °C in pH-buffered organic acids and distilled water. *Tectonophysics* **295**, 93–115.

House, W.A., Orr, D.R., 1992. Investigation of the PH-dependence of the kinetics of quartz dissolution at 25 °C. *J. Chem. Soc. Farad. Trans.* **88**, 233–241.

Jendoubi, F., Mgaidi, A., El Maaoui, M., 1998. The dissolution kinetics of sand as function of particle size. *Can. J. Chem. Eng.* **76**, 233–238.

Koretsky, C.M., Sverjensky, D.A., Sahai, N., 1998. A model of surface site types on oxide and silicate minerals based on crystal chemistry: implications for site types and densities, multi-site adsorption, surface infrared spectroscopy, and dissolution kinetics. *Am. J. Sci.* **298**, 349–438.

Koretsky, C.M., Sverjensky, D.A., Salisbury, J.W., Daria, D.M., 1997. Detection of surface hydroxyl species on quartz, γ-alumina, and feldspars using diffuse reflectance infrared spectroscopy. *Geochim. Cosmochim. Acta* **61**, 2193–2210.

Liu, M., Yund, R.A., Tullis, J., Topor, L., Navrotsky, A., 1995. Energy associated with dislocations—a calorimetric study using synthetic quartz. *Phys. Chem. Mineral.* **22**, 67–73.

Mullins, W.W., Hirth, J.P., 1963. The microscopic kinetics of step motion in growth processes. *Int. J. Phys. Chem. Solid.* **24**, 1391–1404.

Reuschle, T., Darot, M., 1996. The α-quartz trigonal symmetry revealed by fracture tests. *Eur. J. Mineral.* **8**, 695–701.

Rignanese, G.M., de Vita, A., Charlier, J.C., Gonze, X., Car, R., 2000. First-principles molecular-dynamics study of the (0001) α-quartz surface. *Phys. Rev. B* **61**, 13250–13255.

Rimstidt, J.D., Barnes, H.L., 1980. The kinetics of silica–water reactions. *Geochim. Cosmochim. Acta* **44**, 1683–1699.

Schlegel, M.L., Nagy, K.L., Fenter, P., Sturchio, N.C., 2002. Structures of quartz (1010)- and (1011)–water interfaces determined by X-ray reflectivity and atomic force microscopy of natural growth surfaces. *Geochim. Cosmochim. Acta* **66**, 3037–3054.

Schulz, M.S., White, A.F., 1999. Chemical weathering in a tropical watershed, Luquillo mountains, Puerto Rico III: quartz dissolution rates. *Geochim. Cosmochim. Acta* **63**, 337–350.

Tester, J.W., Worley, W.G., Robinson, B.A., Grigsby, C.O., Feerer, J.L., 1994. Correlating quartz dissolution kinetics in pure water from 25 to 625 °C. *Geochim. Cosmochim. Acta* **58**, 2407–2420.

Wagner, T., Jochum, J., 2002. Fluid–rock interaction processes related to hydrothermal vein-type mineralization in the Siegerland district, Germany: implications from inorganic and organic alteration patterns. *Appl. Geochem.* **17**, 225–243.

Xiao, Y.T., Lasaga, A.C., 1996. Ab initio quantum mechanical studies of the kinetics and mechanisms of quartz dissolution: OH^- catalysis. *Geochim. Cosmochim. Acta* **60**, 2283–2295.